

# Characteristics of the Single Active Bridge Converter with Voltage Doubler

Andreas Averbeg\*, Axel Mertens†

Leibniz University Hannover,

Institute for Drive Systems and Power Electronics, Hannover, Germany

\*e-mail: [averberg@ial.uni-hannover.de](mailto:averberg@ial.uni-hannover.de)

†e-mail: [mertens@ial.uni-hannover.de](mailto:mertens@ial.uni-hannover.de)

**Abstract**—This paper investigates the single active bridge dc-dc converter with voltage doubler. An analytical investigation is given, completely describing the operating behaviour of the converter. Herewith, the impact of the transformer's properties and a calculation of the current stress of the semiconductors and passive devices is shown. The results are compared to the single active bridge with full bridge rectifier. With regard to a small ripple current at the converter input, the results can be used as a tool for an optimised converter design. All results are compared to simulations. A 1.2 kW prototype was built, and measurement results are given.

**Keywords**—DC power supply, Fuel cell system, High frequency power converter.

## I. INTRODUCTION

Due to environmental sustainability, nowadays renewable energy becomes more and more important. Fuel cells are only one option for the future. At medium power levels they have a relatively low output voltage, a high output current and large variations in output voltage under variable load conditions [1], [2], [3]. In order to make fuel cells usable for applications with a higher voltage demand, a dc-dc converter with high voltage gain can be used. Many dc-dc converters have been proposed and investigated during the last decade [4]. In [5], an overview of different single phase topologies for small distributed power generators is given. For fuel cell applications, a voltage-fed full bridge, operating with a high transmission ratio transformer, and full bridge rectifier are proposed for single stage converters [6], [7], [8] or two stage converters with a boost converter connected upstream [9]. In [10], the transformer's leakage inductance is used for voltage boosting by substituting two rectifier diodes with IGBTs.

However, the transformer's winding ratio and its leakage inductance affect the operating behaviour of the topology, hence the value of the output voltage, which is investigated in [8]. It is shown in [11], that the transformer's transmission ratio should be held as small as possible to receive a good efficiency of the converter. Thus, the single active bridge converter with voltage doubler rectifier might be a further alternative. In [12], an overview of circuit topologies with voltage doubler rectifier is given. For a fuel cell application, a converter with voltage doubler is used in [13].

This paper deals with the single active bridge converter with voltage doubler shown in Fig. 1, operating

with a phase-shifted pwm. A full analytical investigation of the converter is given. Herewith, the impact of the transformer's winding ratio and its leakage inductance on the operating behaviour of the topology is shown. The current stress of the passive components as well as of all semiconductor devices is emphasised and compared to the single active bridge with full bridge rectifier. All results are proved by simulations. A 1.2 kW prototype was built and experimental results are given in this paper. In the

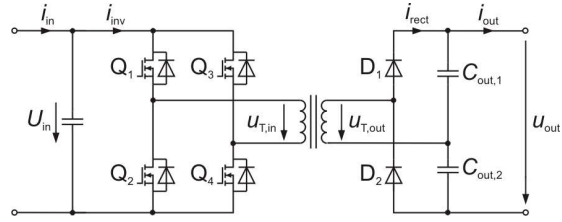


Fig. 1. Single active bridge converter with voltage doubler SAB.VD

following, the single active bridge converter with voltage doubler rectifier is denoted as SAB.VD. The analytical and experimental results are compared to the single active bridge converter with full bridge rectifier. This converter has two diodes instead of the capacitors  $C_{out,1}$  and  $C_{out,2}$  in its rectifier circuit. It is denoted as SAB.FB in this paper and shown in Fig. 2.

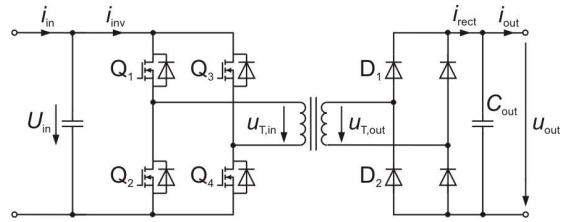


Fig. 2. Single active bridge converter with full bridge rectifier SAB.FB

## II. ANALYSIS OF THE CONVERTER

When modeling the high frequency transformer by its leakage inductance only, the equivalent circuit diagram shown in Fig. 3 is obtained. All secondary values have to be referred to the primary side. Two different operating modes can be distinguished. In the discontinuous conduction mode (DCM), the rectifiers output current

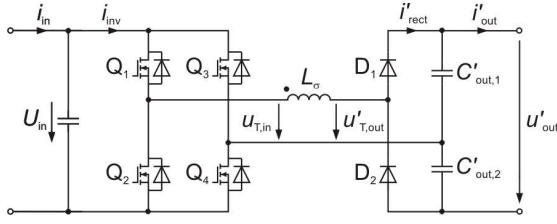


Fig. 3. Equivalent circuit diagram of the SAB.VD

$i'_{\text{rect}}$  is zero for more than one moment during the first half period. During  $0 < t < \frac{T}{2}$ ,  $i'_{\text{rect}}$  is equal to the current through the leakage inductance  $i_{L,\sigma}$ , which is shown in Fig. 4 (a). During  $\frac{T}{2} < t < T$ ,  $i'_{\text{rect}}$  is zero. In Fig. 4 (a), additionally the voltage waveforms of the transformer's input and output voltage  $u_{T,\text{in}}$  and  $u'_{T,\text{out}}$  as well as the output voltage  $u'_{\text{out}}$  are given. The second operating mode is at the border between continuous and discontinuous conduction mode and denoted as border mode (BM). Fig. 4 (b) shows the waveforms. During the time  $t_1 < t < (\frac{T}{2} + t_1)$ , the rectifier current is equal to  $i_{L,\sigma}$ . For the remaining time,  $i'_{\text{rect}}$  is zero. The continuous conduction mode (CCM) does not exist for this converter due to the absent inductor at the converter output. By

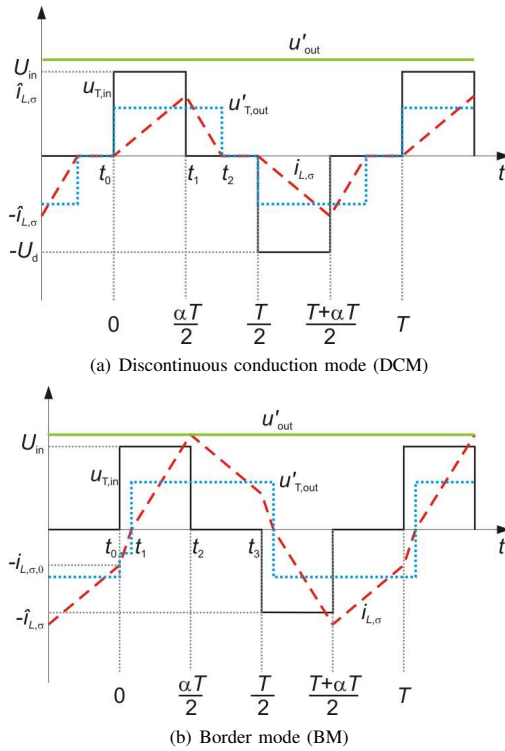


Fig. 4. Voltage and current waveforms

using the waveforms given in Fig. 4 and considering the conducting devices for every single section in both operating modes, the output voltages of the topology can be calculated.

In BM, the first half period can be divided into three different states. At  $t = 0$ , switches  $Q_1$  and  $Q_4$  are closed, switches  $Q_2$  and  $Q_3$  are open. The current through the leakage inductance  $i_{L,\sigma}$  is negative, hence the body diodes  $D_{Q,1}$  and  $D_{Q,4}$  are conducting. Fig. 5 is obtained.

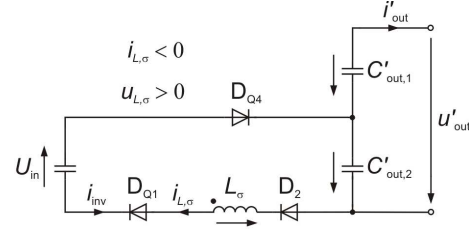


Fig. 5. Border mode, state 1

The current  $i_{L,\sigma}(t)$  can be calculated as:

$$i_{L,\sigma}(t) = i_{L,\sigma}(0) + \frac{U_{\text{in}} + u'_{C,\text{out},2}}{L_\sigma} \cdot t$$

$$0 = i_{L,\sigma}(0) + \frac{U_{\text{in}} + 0.5 \cdot u'_{\text{out}}}{L_\sigma} \cdot t_1 \quad (1)$$

At  $t = t_1$ , the current  $i_{L,\sigma}$  crosses zero. For  $t_1 < t < \frac{\alpha T}{2}$ ,  $Q_1$  and  $Q_4$  are conducting and state 2 (Fig. 6) is active.

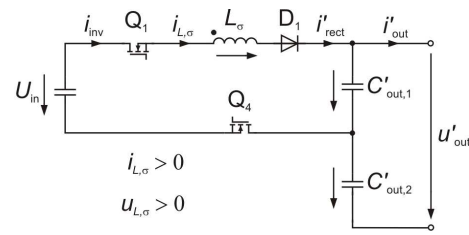


Fig. 6. Border mode, state 2

It is obtained:

$$i_{L,\sigma}(t) = \frac{U_{\text{in}} - u'_{C,\text{out},1}}{L_\sigma} \cdot (t - t_1)$$

$$i_{L,\sigma}\left(\frac{\alpha T}{2}\right) = \frac{U_{\text{in}} - 0.5 \cdot u'_{\text{out}}}{L_\sigma} \left(\frac{\alpha \cdot T}{2} - t_1\right) \quad (2)$$

When  $\alpha$  is the converter's duty cycle, at  $t = \frac{\alpha T}{2}$ ,  $Q_4$  will be turned off and  $Q_3$  will be turned on. The current commutates to the body diode  $D_{Q,3}$  and  $u_{T,\text{in}}$  turns to zero. State 3 is shown in Fig. 7.

It is received:

$$i_{L,\sigma}(t) = i_{L,\sigma}\left(\frac{\alpha T}{2}\right) - \frac{u'_{C,\text{out},1}}{L_\sigma} \cdot \left(t - \frac{\alpha T}{2}\right)$$

$$i_{L,\sigma}\left(\frac{T}{2}\right) = i_{L,\sigma}\left(\frac{\alpha T}{2}\right) - \frac{0.5 \cdot u'_{\text{out}}}{L_\sigma} \cdot (1 - \alpha) \cdot \frac{T}{2} \quad (3)$$

In the stationary case, it is obtained:

$$-i_{L,\sigma}\left(\frac{T}{2}\right) = i_{L,\sigma}(0) \quad (4)$$

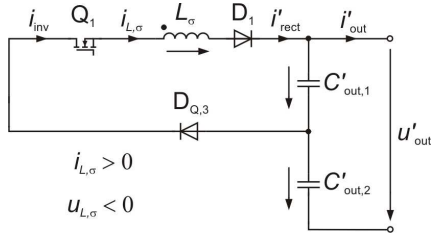


Fig. 7. Border mode, state 3

$Q_1$  will be turned off and  $Q_4$  will be turned on at  $t = t_3 = \frac{T}{2}$ . The same considerations can be done for the second half period. By solving the equations (1) to (4), expressions for the three unknown variables  $i_{L,\sigma}(0)$ ,  $i_{L,\sigma}(\frac{\alpha T}{2})$  and  $t_1$  can be found. Herewith, the converter output current can be calculated as:

$$i'_{out} = \frac{1}{T} \cdot \int_{t_1}^{\frac{T}{2} + t_1} i_{L,\sigma} dt$$

$$i'_{out} = \frac{U_{in}^2 \cdot (2 - \alpha) \cdot \alpha - (0.5 \cdot u'_{out})^2}{16 \cdot f \cdot L_{\sigma} \cdot U_{in}} \quad (5)$$

Rearranging this equation and converting the referred values back to the secondary side leads to the output voltage

$$u_{out,BM} = \frac{2}{N} \sqrt{(2 - \alpha) \cdot \alpha \cdot U_{in}^2 - 16 \cdot f \cdot \frac{i'_{out}}{N} \cdot U_{in} \cdot L_{\sigma}} \quad (6)$$

where  $N$  is the winding ratio  $\frac{w_1}{w_2}$ . The same calculations can be done for the DCM. The result is

$$u_{out,DCM} = \frac{2}{N} \cdot \frac{\alpha^2 \cdot U_{in}^2}{\alpha^2 \cdot U_{in} + 8 \cdot f \cdot \frac{i'_{out}}{N} \cdot L_{\sigma}} \quad (7)$$

It becomes obvious that the leakage inductance causes a voltage drop at the converter's output which rises with the switching frequency and the load current.

In [8], the SAB.FB was investigated. The equations for the output current in BM and DCM are as follows:

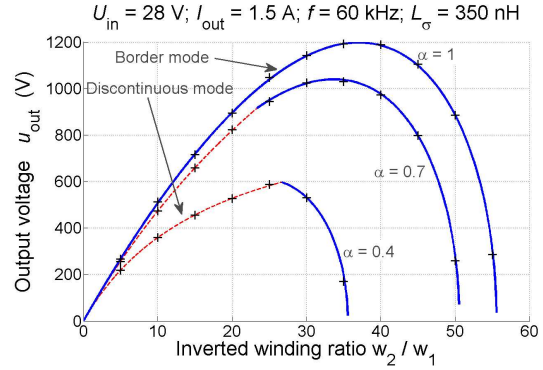
$$u_{out,BM} = \frac{1}{N} \sqrt{(2 - \alpha) \cdot \alpha \cdot U_{in}^2 - 8 \cdot f \cdot \frac{i'_{out}}{N} \cdot U_{in} \cdot L_{\sigma}} \quad (8)$$

$$u_{out,DCM} = \frac{1}{N} \cdot \frac{\alpha^2 \cdot U_{in}^2}{\alpha^2 \cdot U_{in} + 4 \cdot f \cdot \frac{i'_{out}}{N} \cdot L_{\sigma}} \quad (9)$$

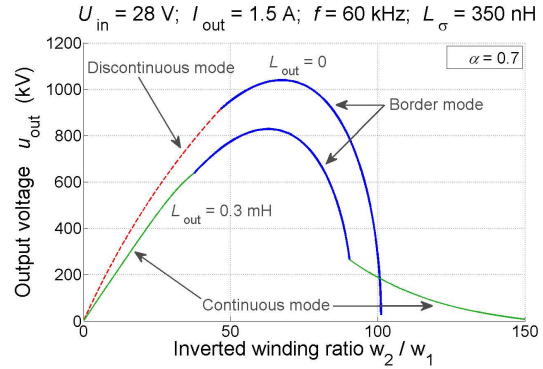
A comparison brings out that the output voltage of SAB.VD is twice the output voltage of SAB.FB for no load conditions only. With rising load current, the voltage drop in the SAB.VD topology is larger than the voltage drop in the SAB.FB topology.

Fig. 8 (a) shows the dependency of the output voltage over the inverted winding ratio of the transformer for three different duty cycles. Further parameters are: input voltage  $U_{in} = 28$  V, output current  $i_{out} = 1.5$  A,

switching frequency  $f = 60$  kHz and leakage inductance  $L_{\sigma} = 350$  nH. As can be seen, a maximum occurs at a special winding ratio, and increasing the number of secondary turns further leads even more to an increased voltage gain. The crosses mark results taken from a simulation. The simulated and calculated results fit exactly. For  $\alpha = 0.7$ , the curve  $u_{out}$  over  $\frac{w_2}{w_1}$  is additionally given for the SAB.FB in Fig. 8 (b). Although no voltage doubler is used, the maximum voltage gain is exactly the same, in this case 1040 V. The SAB.FB offers the possibility to insert an output inductor  $L_{out}$ . For the sake of completeness, in Fig. 8 (b)  $u_{out}$  over  $\frac{w_2}{w_1}$  is also given for  $L_{out} = 0.3$  mH. In this case, the continuous conduction mode CCM may occur.



(a) SAB.VD



(b) SAB.FB

Fig. 8. Output voltage over inverted winding ratio

As can be shown, the maximum voltage gain is obtained always in BM or at the border between BM and DCM. It is possible to find the winding ratio which gives the best voltage gain by building the derivation of (6), and set it to zero. Equation (10) is obtained.

$$\frac{1}{N_{opt}} = \frac{1}{12} \cdot \frac{U_{in} \cdot \alpha \cdot (2 - \alpha)}{i_{out} \cdot f \cdot L_{\sigma}} \quad (10)$$

$N_{opt}$  is the winding ratio, which leads to the highest overall voltage gain. By inserting equation (10) into (6), the maximum possible output voltage for a given output

current can be calculated.

$$U_{\text{out,max}} = \frac{\sqrt{3}}{36} \cdot \frac{U_{\text{in}}^2 \cdot \alpha \cdot (2 - \alpha) \cdot \sqrt{(\alpha \cdot (2 - \alpha))}}{i_{\text{out}} \cdot f \cdot L_{\sigma}} \quad (11)$$

Fig. 9 shows the curve progressions of the maximum reachable output voltage over the output current for four different leakage inductances. Fig. 9 is valid for both, SAB\_VD and SAB\_FB. When using SAB\_FB with an additional output inductor, the results can be slightly different due to CCM operation of the converter. This is shown in [8]. Multiplying  $u_{\text{out}}$  with  $i_{\text{out}}$  gives the output power, which is also shown in Fig. 9. Since in (11)  $i_{\text{out}}$

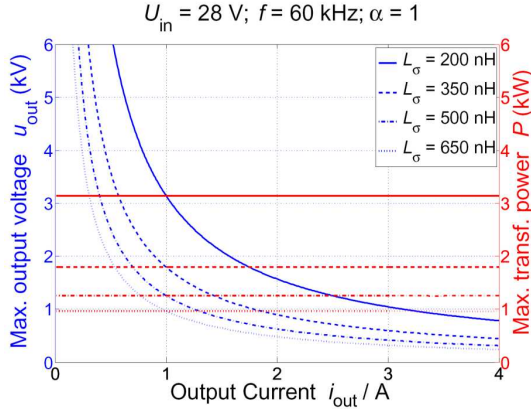


Fig. 9. Maximum values of output voltage and transferred power

only appears in the denominator, the maximum output power over the whole current range is constant. This means, the voltage drop across the leakage inductance due to high frequency operation limits the possible output power of the converter for a given output current.

### III. EFFICIENCY OF THE CONVERTER

#### A. Dispartment of the loss mechanisms

As described in section II, by solving the equations (1) to (4), expressions for the three unknown variables  $i_{L,\sigma}(0)$ ,  $i_{L,\sigma}(\frac{\alpha T}{2})$  and  $t_1$  can be found. By inserting equation (6), the duty cycle  $\alpha$  can be eliminated. The results can be used for pre-estimating mean values and rms values of the semiconductor currents, the semiconductors' turn off currents and finally the converter's efficiency in dependency of the output power in the form of  $i_{\text{out}}$  and  $u_{\text{out}}$ . This is presented here for the BM.

Fig. 10 shows the voltage and current waveforms of the switches  $Q_1$  to  $Q_4$  for BM. If the MOSFET of switch  $Q_x$  is conducting, it is marked by an index M:  $i_{M,x}$ , if the anti-parallel body diode is conducting, it is marked by an index B:  $i_{B,x}$ . Due to the phase-shifted pwm, all mean and rms values of the switches  $Q_1$  and  $Q_2$  are equal and all mean and rms values of the switches  $Q_3$  and  $Q_4$  are equal, too.

Typically, a MOSFET has a better on-state resistance  $R_{\text{DS,on}}$  than its intrinsic body diode. For this reason, it is expedient to distinguish between the MOSFET's current

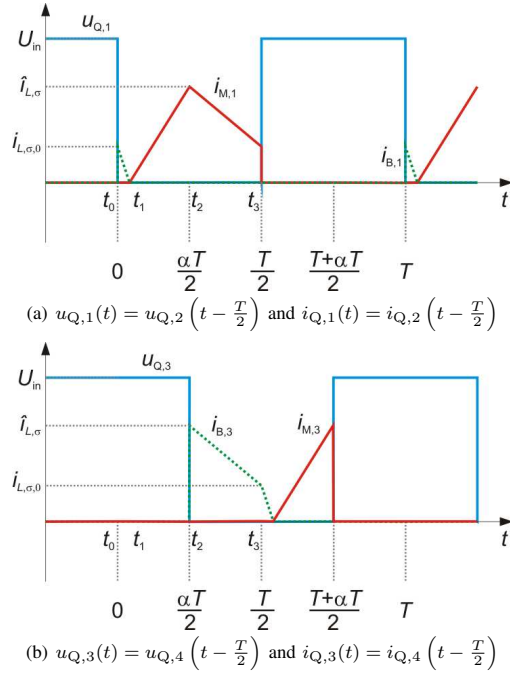


Fig. 10. Voltage and current waveforms of the switches  $Q_1$  to  $Q_4$  in BM

$i_M$  and the current through its body diode  $i_B$ . With the knowledge of the current waveforms of Fig. 10 and the calculated characteristic values of section II, it is possible to calculate the current mean values individually. The results for the switch  $Q_1$  are given in equations (12) and (13). The variable  $X$  stands for the triple  $f \cdot L_{\sigma} \cdot i_{\text{out}}$ . The same calculations can be accomplished for the rms values. Since the calculation for  $I_{M,1}$  results in a long term, only  $I_{B,1}$  is shown in (14). Equation (15) arises for the turn off current of switch  $Q_1$ .

The currents for the other switches as well as the currents through the rectifier diodes can be calculated analogously. With the described method, expressions for the currents are obtained, which depend only on the pre-known parameters  $I(U_{\text{in}}, u_{\text{out}}, i_{\text{out}}, f, L_{\sigma}, N)$ .

To pre-estimate the transformer's copper losses, the current  $i_{L,\sigma}$  has to be calculated, which can be done as before. Furthermore, iron losses appear in the transformer, which are a function of the magnetic flux density  $B_{\mu}$  and the switching frequency  $f$ . When  $B_{\mu}$  and  $f$  are known, they can be taken from the core material's data sheet.

$$P_{\text{Fe}} = f(B_{\mu}, f) \cdot V_{\text{Fe}} \quad (16)$$

Here  $V_{\text{Fe}}$  is the transformer's volume,  $A_{\text{Fe}}$  is its cross section. The magnetic flux density can be substituted by the magnetomotive force, which is the integral of the transformer input voltage  $u_{T,\text{in}}$  over one half period.

$$B_{\mu} = \frac{\psi_{\mu}}{w_1 \cdot A_{\text{Fe}}} \quad (17)$$

$$\bar{i}_{M,1} = \frac{\left(U_{in}^2 - \frac{u_{out} \cdot N}{2}\right) \sqrt{U_{in}^2 - 16 \cdot U_{in} \cdot \frac{X}{N} - \left(\frac{u_{out} \cdot N}{2}\right)^2} - U_{in}^3 + 8U_{in} \left(3 \cdot U_{in} \frac{X}{N} + \frac{u_{out} \cdot N}{2}\right) + U_{in} \left(\frac{u_{out} \cdot N}{2}\right)^2}{16 \cdot U_{in}^2 \cdot f \cdot L_{\sigma}} \quad (12)$$

$$\bar{i}_{B,1} = \frac{\left(\sqrt{U_{in}^2 - 16 \cdot U_{in} \cdot \frac{X}{N} - \left(\frac{u_{out} \cdot N}{2}\right)^2} - U_{in} + \frac{u_{out} \cdot N}{2}\right)^2 \cdot \left(U_{in} + \frac{u_{out} \cdot N}{2}\right)}{32 \cdot U_{in}^2 \cdot f \cdot L_{\sigma}} \quad (13)$$

$$I_{B,1} = \frac{\sqrt{3}}{24} \cdot \sqrt{\frac{\left(U_{in} - \sqrt{U_{in}^2 - 16U_{in} \frac{X}{N} - \left(\frac{u_{out} \cdot N}{2}\right)^2} - \frac{u_{out} \cdot N}{2}\right)^3 \cdot \left(U_{in} + \frac{u_{out} \cdot N}{2}\right)^2}{U_{in}^3 \cdot f^2 \cdot L_{\sigma}^2}} \quad (14)$$

$$i_{Q,1,off} = i_{L,\sigma}(0) = \frac{\left(\sqrt{U_{in}^2 - 16U_{in} \frac{X}{N} - \left(\frac{u_{out} \cdot N}{2}\right)^2} - U_{in} + \frac{u_{out} \cdot N}{2}\right) \cdot \left(U_{in} + \frac{u_{out} \cdot N}{2}\right)}{4 \cdot U_{in} \cdot f \cdot L_{\sigma}} \quad (15)$$

$$\psi_{\mu} = \frac{1}{2} \cdot \int_0^{\frac{\pi}{2}} u_{T,in}(t) dt = \frac{\alpha}{4 \cdot f} \cdot U_{in} \quad (18)$$

This leads to

$$P_{Fe} = f \left( \frac{\alpha \cdot U_{in}}{4 \cdot f \cdot w_1 \cdot A_{Fe}} \right) \cdot V_{Fe} \quad (19)$$

As before, equations (6) and (7), respectively can be used to eliminate the variable  $\alpha$ , which is not known automatically. An expression

$$P_{Fe} = f(U_{in}, u_{out}, i_{out}, f, L_{\sigma}, N, w_1, A_{Fe}, V_{Fe}) \quad (20)$$

is obtained.

With these equations, all main losses of the converter can be pre-estimated.

### B. The converter in a fuel cell application

In fuel cell systems, the converter input voltage, which is equal to the fuel cell output voltage, depends on the instant power. Loading the fuel cell leads to a reduced output voltage. The crosses in Fig. 11 mark measured values of the output voltage of a 1.2 kW Nexa fuel cell stack [14]. The ideal open circuit potential of one

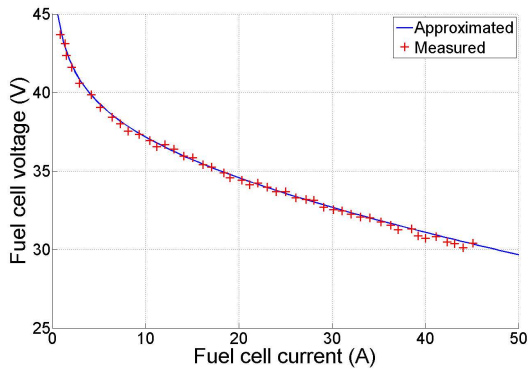


Fig. 11. Characteristic curve of the Nexa fuel cell system

single cell is given by the Nernst potential  $E$ . During

operation, activation related losses  $\eta_{act}$ , ohmic losses  $\eta_{ohm}$  and mass transport related losses  $\eta_{conc}$  occur. These loss mechanisms depend on the fuel cell's current [1].

$$u_{FC}(i_{FC}) = \text{Number of Cells} \cdot (E - \eta_{act}(i_{FC}) - \eta_{ohm}(i_{FC}) - \eta_{conc}(i_{FC})) \quad (21)$$

Based on (21), a mathematical model for the fuel cell output voltage was built. The solid line in Fig. 11 shows the approximated characteristic.

By interlinking the mathematical model of the fuel cell with the mathematical model of the converter, the characteristics of the complete system can be investigated. The upper graphs in Fig. 12 show the calculated development of the converter losses over the output power when it is connected to the fuel cell system. Due to the pure analytic investigation, the calculation is extremely fast. It takes only a few seconds to get the results for the predicted losses over the full range of power.

In this case, the switching frequency is  $f = 60$  kHz and the leakage inductance  $L_{\sigma} = 308$  nH. The output voltage is held on a constant level of  $u_{out} = 600$  V. The losses are divided into rectifier losses, transformer losses, inverter switching losses and inverter ohmic losses. Four different cases are given. The number of primary windings  $w_1$  is 2, the number of secondary windings  $w_2$  varies from 23 to 26, hence  $\frac{1}{N}$  varies from 11.5 to 13. As can be seen, over the whole power range, the topology with the smallest number of secondary turns brings out the best efficiency. This is due to a higher duty cycle  $\alpha$  which is given in the lower graph of Fig. 12. Having equal current mean values, a higher duty cycle results in lower values of the effective currents and lower turn off currents. Accordingly, the inverter losses decrease. Coinstantaneously, a higher duty cycle results in a higher transformer voltage stress, leading to higher transformer losses. But in this case, the over all losses decrease. As can be seen in the course of  $\alpha$ , the reserve for  $\frac{1}{N} = 11.5$  is little (for nominal power  $P = 1200$  W,  $\alpha$  is nearly 1). For this reason, the inverted winding ratio of the prototype was chosen to 12.



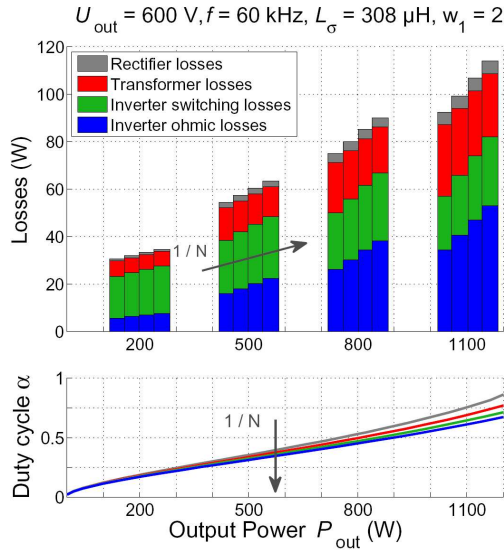


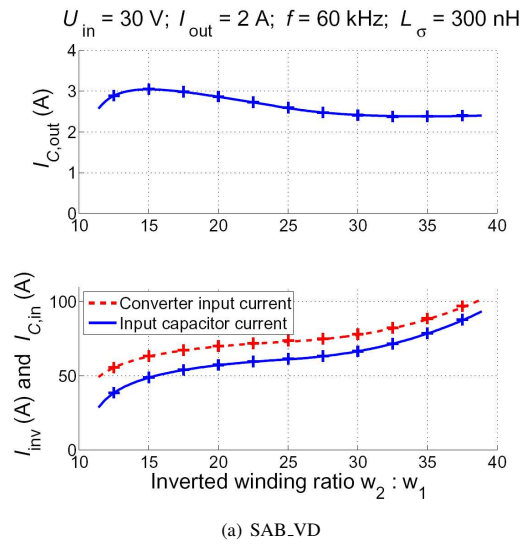
Fig. 12. Efficiency over the input current

#### IV. RIPPLE CURRENT

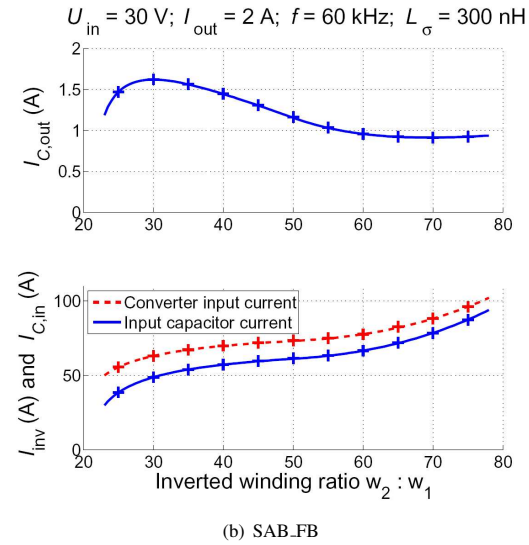
The effect of inverter ripple current on fuel cell stack performance and stack lifetime remains uncertain. In [15], it is mentioned that at least converter frequencies under 120 Hz or ripple factors above 4 % have a negative impact on the fuel cell. The double layer capacitor of the fuel cell can be used to smooth the current only up to a certain rms value as described in [16]. However, it remains to be useful to be able to calculate this current. In the following, the behaviour of the inverter input current  $i_{inv}$  is described under different topology parameters. This current is equal to the fuel cell's current when using no input capacitor. Otherwise, the input capacitor smooths the input current and provides a current ripple itself. Due to the fact, that a high rms current results in a larger operating temperature which leads - especially for electrolytic capacitors - to shorter capacitor lifetimes, the input and output capacitors' rms currents are calculated, too.

For a given output power, the mean values of the specific converter currents, e.g.  $i_{inv}$  or  $i_{L,\sigma}$  are the same, independent of the other topology parameters. The rms values of these currents vary due to the different current ripples. Hence, the rms value is a quantity for the current ripple. These values can be achieved as described in section III-A.

The calculated rms current at the upper output capacitor  $C_{out,1}$  is shown in the upper graph of Fig. 13 (a). The rms current of  $C_{out,2}$  is the same. The lower graphs show the rms currents at the converter input and at the input capacitor. Simulations are done to prove the calculations. Their results are marked by the crosses. The assumed parameters are an input voltage of  $U_{in} = 30$  V, an output voltage of  $u_{out} = 600$  V, an output current of  $i_{out} = 2$  A and a leakage inductance of  $L_\sigma = 300$  nH. The switching



(a) SAB.VD



(b) SAB.FB

Fig. 13. rms currents of input and output capacitor and inverter rms current

frequency is  $f = 60$  kHz. As can be seen, for small winding ratios,  $I_{C,out}$  is about 3 A. It becomes lower with increasing winding ratio. The currents at the converter input evolve contrarily. Due to the fact that fuel cell converters have a large input current and small output current, besides the findings in [8], [11] and section III-B, this is another reason to implement a winding ratio as small as possible.

To give a comparison to the SAB.FB topology, in Fig. 13 (b) the same curves are shown for the SAB.FB again. As before, the crosses mark simulation results to approve the calculations. Besides the fact that the winding ratio is doubled, the input currents are exactly the same. The current  $I_{C,out}$  is smaller but not exactly halved. The curve shows the same trend but in a wider range.

## V. TRANSFORMER DESIGN

For the transformer an ETD/59/31/22 core was used. To identify a reasonable winding ratio, ten transformers with different winding ratios are built. The development of  $L_\sigma$  with rising numbers of secondary turns  $w_2$  is given in Fig. 14 for ten transformers. As can be seen, this is a slightly linear rising curve. In section II, it is presented

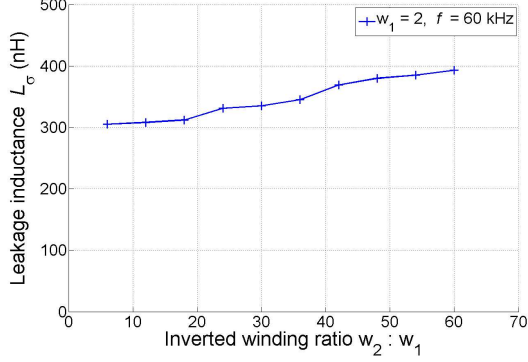


Fig. 14. Measured leakage inductance for a transformer with various secondary turns

how the leakage inductance influences the operating behaviour of the converter. Especially for applications with high voltage gain, it is important to reduce the leakage inductance  $L_\sigma$  as far as possible. In section III-B, it is stated out, that a small inverted winding ratio brings out a good efficiency. This fits to the course of  $L_\sigma$ .

Compared to the SAB\_FB, the inverted winding ratio of the SAB\_VD can be halved, hence a slightly smaller leakage inductance occurs. On the other hand, the voltage drop due to the high frequency operation is higher for the SAB\_VD (cp. equations (6), (8) and (7), (9) respectively). However, the transformer's volume and its losses for both topologies are the same. The iron losses are a function of the magnetic flux density  $B_\mu$  which can be calculated by equation (18). When the secondary turns are halved due to the voltage doubler, the duty cycle  $\alpha$  has to be the same as in the SAB\_FB leading to the same magnetic flux density, hence to the same iron losses. Since the current in the secondary turns of the SAB\_VD will be twice the current in the SAB\_FB, the copper area has to be doubled, which leads to a similar transformer volume.

## VI. EXPERIMENTAL RESULTS

For the single active bridge with voltage doubler, a 1.2 kW prototype was built. Parameters of the important electrical devices can be taken from I. Based on the findings of section III-B and V respectively, the transformer's winding ratio is chosen to  $\frac{w_1}{w_2} = \frac{2}{24}$ . This corresponds to a leakage inductance  $L_\sigma = 308$  nH. For the two output capacitors, the transformer's magnetizing current achieves a balancing effect depending on its negative feedback [17].

Measured voltage and current waveforms for the discontinuous operating modes are shown in Fig. 15 (a).

TABLE I  
PARAMETERS OF THE PROTOTYPE

Inverter		Rectifier		Transformer	
$R_{DS,on}$	4.5 m $\Omega$	$R_{F,D}$	50 m $\Omega$	$A_{Fe}$	368 mm <sup>2</sup>
$R_{F,B}$	5 m $\Omega$	$U_{F,D}$	1 V	$V_{Fe}$	51200 mm <sup>3</sup>
$U_{F,B}$	0.5 V				
$Q_{GS}$	46 nC				
$Q_{GD}$	65 nC				
$U_{Gate}$	15 V				
$R_{Gate}$	5 $\Omega$				

These are the transformer input voltage  $u_{T,in}$  and input current  $i_{T,in}$ , which is equal to  $i_{L,\sigma}$ , when neglecting the transformer's magnetizing current. Furthermore, the output voltage is given. Fig. 15 (b) shows the waveforms for the border mode. For the transformer input current,

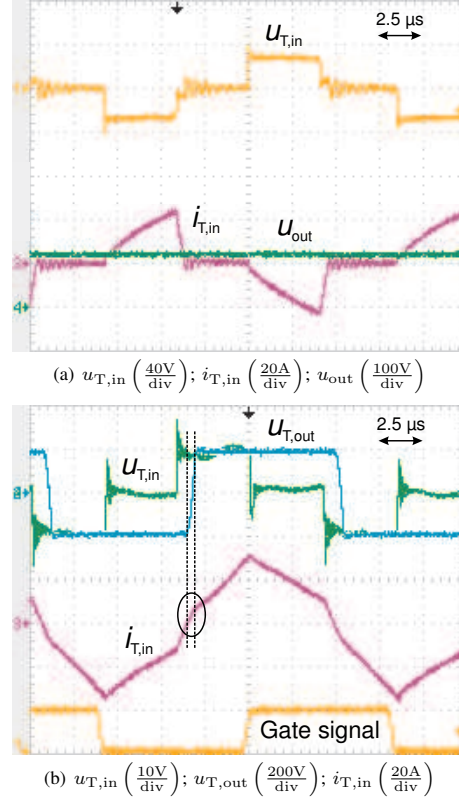


Fig. 15. Current and voltage waveforms in the two operating modes

there is one difference to the ideal waveform marked by the circle in Fig. 15 (b). An offset in  $i_{T,in}$  occurs. The reason might be the charging time at the rectifier diodes as can be seen in the waveform of  $u_{T,out}$ .

The converter was connected to a NEXA fuel cell system [14]. As described in section III-B, this fuel cell system has an output voltage in a range of 44 V at no load down to 31 V and 40 A at full load (cp. Fig. 11). In the upper graph of Fig. 16, the measured efficiency of the converter is given when it is supplied by the fuel cell voltage. The output voltage is held on a constant value of  $u_{out} = 600$  V. Under full load, the voltage gain is

$\frac{600\text{ V}}{31\text{ V}} = 19.4$ . The efficiency reaches 92.7 %. The dashed line shows the calculated efficiency, using the analytic results from section II. As can be seen, calculated and experimental results fit reasonably well.

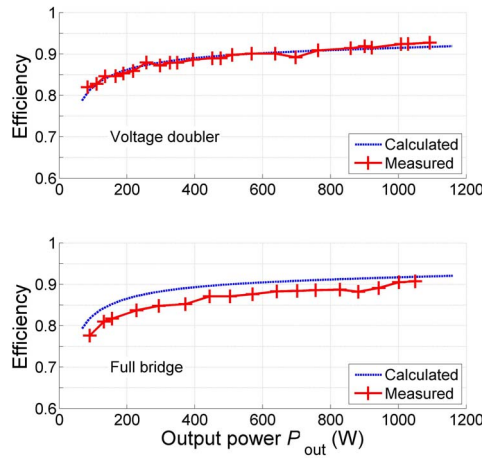


Fig. 16. Efficiency over the output power

In [11], an analytic investigation of the single active bridge with full bridge rectifier is given. Based on these results, the efficiency of the SAB\_FB was calculated when using the same devices as for the SAB\_VD. The only difference is the number of secondary transformer turns  $w_2 = 48$ . The result of the calculation is presented in the lower graph of Fig. 16. Both calculated efficiencies of SAB\_VD and SAB\_FB respectively, are nearly the same. Additionally, measured results taken from a prototype of the SAB\_FB are shown, which was built with the same devices as the prototype of the SAB\_VD. The experimental results are marked by the crosses. The trend fits to the calculation, but the measured curve shows a slightly lower efficiency in the range of approximately two percent.

## VII. CONCLUSION

In this paper, a complete analytic investigation of the single active bridge with voltage doubler is presented. Both possible operating modes DCM and BM are involved into the analysis. Based on the results, the maximum voltage gain and the maximum power which can be transferred by this topology are emphasised. These values depend on the leakage inductance and the converter's switching frequency. Furthermore, a tool for pre-estimating the converter losses divided in the several loss mechanisms is presented. Due to the pure analytic investigation, this tool is extremely fast. The benefits of this tool are shown for the converter working in a fuel cell system. All calculations are approved by simulation results. The impact of the transformer's winding ratio on the converter's current ripple as well as on the input and output capacitors is stated out. A prototype is built and experimental results for the converter working in a

fuel cell system are given. At a voltage gain of 19.4, an efficiency of 92.7 % is reached. Furthermore, all results are compared to the single active bridge with full bridge rectifier.

## REFERENCES

- [1] W. Vielstich, H. A. Gasteiger, and A. Lamm, *Handbook of Fuel Cells - Fundamentals, Technology and Applications*. John Wiley and Sons, Ltd., 2003, vol. 1: Fundamentals and Survey of Systems.
- [2] R. Ramakumar, "Fuel cells-an introduction," in *Power Engineering Society Summer Meeting, 2001. IEEE*, vol. 1, July 2001.
- [3] M. Ellis, M. Von Spakovsky, and D. Nelson, "Fuel cell systems: efficient, flexible energy conversion for the 21st century," *Proceedings of the IEEE*, vol. 89, no. 12, pp. 1808–1818, Dec. 2001.
- [4] M. Aydemir, A. Bendre, and G. Venkataramanan, "A critical evaluation of high power hard and soft switched isolated dc-dc converters," in *Industry Applications Conference, 2002. 37th IAS Annual Meeting. Conference Record of the*, vol. 2, 13–18 Oct. 2002, pp. 1338–1345vol.2.
- [5] Y. Xue, L. Chang, S. B. Kjr, J. Bordonau, and T. Shimizu, "Topologies of single-phase inverters for small distributed power generators: An overview," in *IEEE Transactions on Power Electronics*, Vol. 19, No. 5, September 2004, 2004, pp. 1305–1314.
- [6] J. Wang, M. Reinhard, F. Peng, and Z. Qian, "Design guideline of the isolated dc-dc converter in green power applications," in *Power Electronics and Motion Control Conference, 2004. IPEMC 2004. The 4th International*, vol. 3, 14–16 Aug. 2004, pp. 1756–1761Vol.3.
- [7] H. Xu, L. Kong, and X. Wen, "Fuel cell power system and high power dc-dc converter," *Power Electronics, IEEE Transactions on*, vol. 19, no. 5, pp. 1250–1255, Sept. 2004.
- [8] A. Averberg and A. Mertens, "Analysis of a voltage-fed full bridge dc-dc converter in fuel cell systems," in *Power Electronics Specialists Conference, 2007. PESC '07. IEEE 38th*, 2007, pp. 286–292.
- [9] J. Lee, J. Jo, S. Choi, and S.-B. Han, "A 10-kw soft low-voltage battery hybrid power conditioning system for residential use," *Energy Conversion, IEEE Transactions on*, vol. 21, no. 2, pp. 575–585, June 2006.
- [10] R. Sharma and H. Gao, "Low cost high efficiency dc-dc converter for fuel cell powered auxiliary power unit of a heavy vehicle," *Power Electronics, IEEE Transactions on*, vol. 21, no. 3, pp. 587–591, May 2006.
- [11] A. Averberg and A. Mertens, "Design considerations of a voltage-fed full bridge dc-dc converter with high voltage gain for fuel cell applications," in *Power Electronics and Applications, 2007 European Conference on*, 2007.
- [12] J. Salmon, "Circuit topologies for single-phase voltage-doubler boost rectifiers," in *Applied Power Electronics Conference and Exposition, 1992. APEC '92. Conference Proceedings 1992., Seventh Annual*, 23–27 Feb. 1992, pp. 549–556.
- [13] J. Wang, F. Peng, J. Anderson, A. Joseph, and R. Buffenbarger, "Low cost fuel cell converter system for residential power generation," *Power Electronics, IEEE Transactions on*, vol. 19, no. 5, pp. 1315–1322, Sept. 2004.
- [14] *Nexa Power Module Users Manual*, Ballard Power Systems Inc., 2003.
- [15] R. S. Gemmen, "Analysis for the effect of inverter ripple current on fuel cell operating condition," in *Transactions of the ASME, Vol. 125*, May 2003, 2003.
- [16] G. Fontes, C. Turpin, R. Saisset, T. Meynard, and S. Astier, "Interactions between fuel cells and power converters influence of current harmonics on a fuel cell stack," in *Power Electronics Specialists Conference, 2004. PESC 04. 2004 IEEE 35th Annual*, vol. 6, 20–25 June 2004, pp. 4729–4735Vol.6.
- [17] Y. Gu, L. Hang, Z. Lu, Z. Qian, and D. Xu, "Voltage doubler application in isolated resonant converters," in *Industrial Electronics Society, 2005. IECON 2005. 32nd Annual Conference of IEEE*, 6–10 Nov. 2005, p. 5pp.